



# Preparation of Acetylenediol (HOCCOH) and Glyoxal (HCOCHO) in Interstellar Analog Ices of Carbon Monoxide and Water

Jia Wang<sup>1,2</sup> , Andrew M. Turner<sup>1,2</sup>, Joshua H. Marks<sup>1,2</sup> , Chaojiang Zhang<sup>1,2</sup>, N. Fabian Kleimeier<sup>1,2</sup>, Alexandre Bergantini<sup>1,2,4</sup> , Santosh K. Singh<sup>1,2</sup>, Ryan C. Fortenberry<sup>3</sup> , and Ralf I. Kaiser<sup>1,2</sup>

<sup>1</sup> W. M. Keck Research Laboratory in Astrochemistry, University of Hawaii at Manoa, Honolulu, HI 96822, USA; [ralfk@hawaii.edu](mailto:ralfk@hawaii.edu)

<sup>2</sup> Department of Chemistry, University of Hawaii at Manoa, Honolulu, HI 96822, USA

<sup>3</sup> Department of Chemistry & Biochemistry, University of Mississippi, MS 38677, USA; [r410@olemiss.edu](mailto:r410@olemiss.edu)

Received 2024 January 27; revised 2024 March 23; accepted 2024 April 7; published 2024 May 21

## Abstract

Enols—tautomers of ketones or aldehydes—are considered key intermediates in the formation of prebiotic sugars and sugar acids. Although laboratory simulation experiments suggest that enols should be ubiquitous in the interstellar medium, the underlying formation mechanisms of enols in interstellar environments are largely elusive. Here, we present the laboratory experiments on the formation of glyoxal (HCOCHO) along with its ynol tautomer acetylenediol (HOCCOH) in interstellar ice analogs composed of carbon monoxide (CO) and water (H<sub>2</sub>O) upon exposure to energetic electrons as a proxy for secondary electrons generated from Galactic cosmic rays. Utilizing tunable vacuum ultraviolet photoionization reflectron time-of-flight mass spectrometry, glyoxal and acetylenediol were detected in the gas phase during temperature-programmed desorption. Our results reveal the formation pathways of glyoxal via radical–radical recombination of two formyl (HĊO) radicals, and that of acetylenediol via keto-enol-ynol tautomerization. Due to the abundance of carbon monoxide and water in interstellar ices, glyoxal and acetylenediol are suitable candidates for future astronomical searches. Furthermore, the detection of acetylenediol in astrophysically relevant ices advances our understanding for the formation pathways of high-energy tautomers such as enols in deep space.

*Unified Astronomy Thesaurus concepts:* [Laboratory astrophysics \(2004\)](#); [Astrochemistry \(75\)](#); [Radical-radical recombination \(1071\)](#); [Complex organic molecules \(2256\)](#); [Interstellar molecules \(849\)](#)

## 1. Introduction

Since the first identification of vinyl alcohol (CH<sub>2</sub>CHOH) in the interstellar medium (ISM) by Turner et al. (Turner & Apponi 2001) two decades ago toward the dense molecular cloud Sagittarius B2(N), enols—alkenes carrying a hydroxyl group at a carbon–carbon double bond—have received considerable attention from the astrochemistry (Abplanalp et al. 2016b; Kleimeier et al. 2021; Kleimeier & Kaiser 2022), synthetic organic chemistry (Mardyukov et al. 2021, 2023), physical chemistry (Taatjes et al. 2005; Rösch et al. 2021; Melosso et al. 2022), and theoretical chemistry (Elango et al. 2010; Ballotta et al. 2023; Mó et al. 2023; Würmel & Simmie 2024) communities. This interest is mainly due to their key role as reactive intermediates in the synthesis of biorelevant molecules related to the *Origins of Life*. 1,2-ethenediol (HOCHCHOH) and 1,1,2-ethenetriol (HOCHC(OH)<sub>2</sub>), the enol forms of glycolaldehyde (HCOCH<sub>2</sub>OH) and glycolic acid (HOCH<sub>2</sub>COOH), respectively, have been proposed as key intermediates leading to the prebiotic formation of three- to five-carbon sugars (Ricardo et al. 2004; Kim et al. 2011; Coggins & Powner 2017) and sugar acids (Mardyukov et al. 2021). Gas-phase enols in the ISM exhibit significantly greater stability (Taatjes et al. 2005; Abplanalp et al. 2016b) because they cannot overcome the high keto-enol tautomerization

barriers (230–290 kJ mol<sup>−1</sup>) at low temperatures and pressures (da Silva 2010; Schreiner et al. 2011; Kleimeier & Kaiser 2021; Wang et al. 2023c).

Among the nearly 300 molecules identified in deep space (McGuire 2022); however, only few enols have been detected. Besides vinyl alcohol, 1,2-ethenediol (HOCHCHOH) has been identified toward the G+0.693–0.027 molecular cloud located in the Galactic Center with a molecular abundance of  $1.3 \times 10^{-10}$  with respect to molecular hydrogen (Rivilla et al. 2022). In addition, 3-hydroxypropenal (HOCHCHCHO), the enol tautomer of malonaldehyde (HCOCH<sub>2</sub>CHO), has been tentatively detected in the ISM toward the solar-type protostar IRAS 16293–2422 (Coutens et al. 2022). On the other hand, laboratory studies on interstellar analog ices revealed a facile formation of enols (Figure 1, Table 1). These results suggest that enols should be ubiquitous in hot cores and star-forming regions and readily available for an abiotic synthesis of complex organic molecules (COMs)—organic molecules containing six or more atoms of carbon, hydrogen, oxygen, or nitrogen (Herbst & Dishoeck 2009)—in an interstellar environment (Wang et al. 2008, 2023b, 2023c; Kleimeier et al. 2020, 2021; Kleimeier & Kaiser 2022). Once formed in molecular clouds, these molecules can sublime into the gas phase in the star-forming region and be incorporated into asteroids and comets (Cooper et al. 2011; Kleimeier et al. 2020). Eventually, parts of enols may survive entry into the atmosphere of other planets such as the early Earth, serving as crucial intermediates in the formation of prebiotic molecules linked to the *Origin of Life* (Benner et al. 2010). Furthermore, a fundamental understanding of the formation of enols and their keto tautomers such as the vinyl alcohol—acetaldehyde pair is of crucial importance as these molecules are considered key

<sup>4</sup> Present address: Centro Federal de Educacao Tecnologica Celso Suckow da Fonseca-CEFET/RJ, Av. Maracana 229, 20271-110, Rio de Janeiro, Brazil.



Original content from this work may be used under the terms of the [Creative Commons Attribution 4.0 licence](#). Any further distribution of this work must maintain attribution to the author(s) and the title of the work, journal citation and DOI.

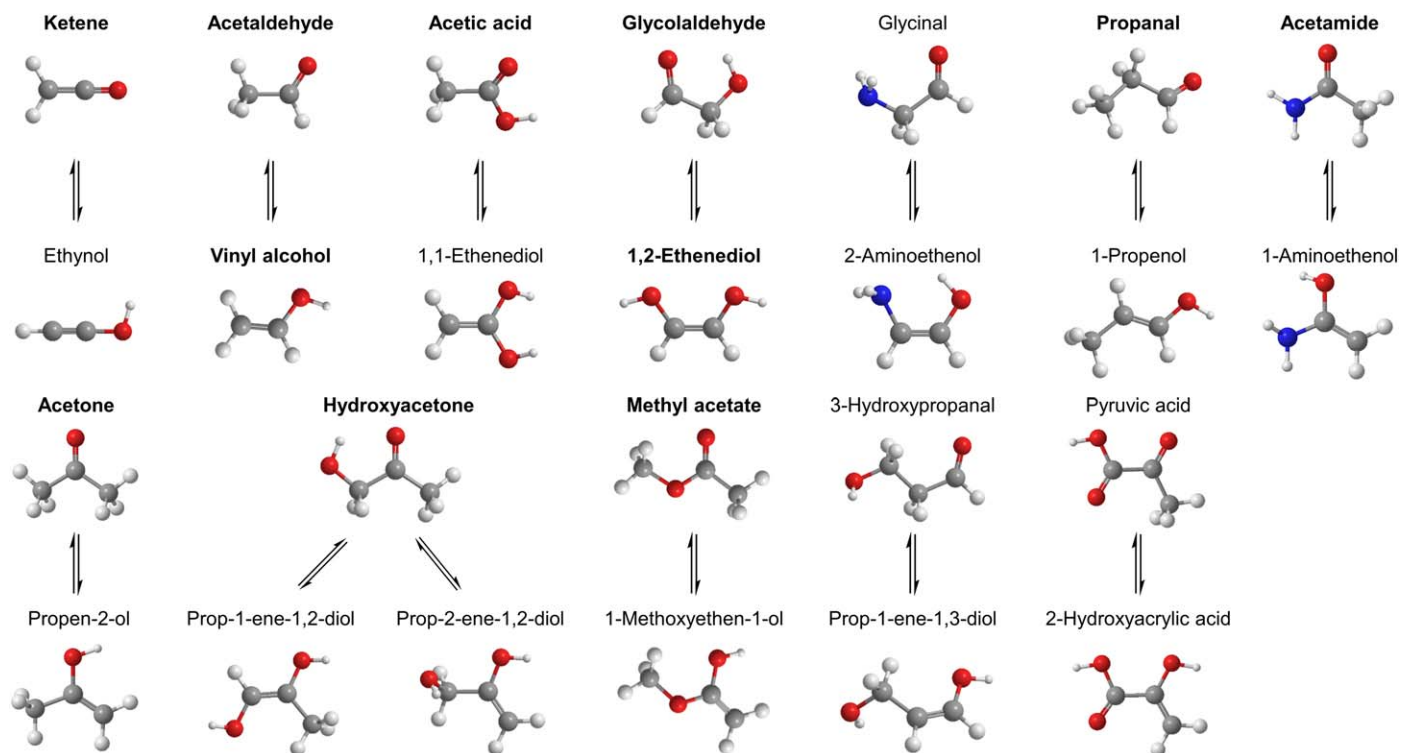


**Figure 1.** Enol tautomers prepared and detected in distinct interstellar analog ices subjected to ionizing radiation. Isomers in bold indicate astronomical detections.

**Table 1**  
The Enols and Ynols Formed in Interstellar Analog Ices Subjected to Ionizing Radiation

No.	Aldehydes or Ketones	Enols or Ynols	$\Delta E$ (kJ mol <sup>-1</sup> )	References
1	ketene (H <sub>2</sub> CCO)	ethynol (HCCOH)	140	Turner et al. (2020)
2	acetaldehyde (CH <sub>3</sub> CHO)	vinyl alcohol (CH <sub>2</sub> CHOH)	41	Abplanalp et al. (2016b), Zhu et al. (2022b)
3	acetic acid (CH <sub>3</sub> COOH)	1,1-ethenediol (H <sub>2</sub> CC(OH) <sub>2</sub> )	112	Kleimeier & Kaiser (2022)
4	glycolaldehyde (HCOCH <sub>2</sub> OH)	1,2-ethenediol (HOCHCHOH)	34	Kleimeier et al. (2021)
5	glycinal (NH <sub>2</sub> CH <sub>2</sub> CHO)	2-aminoethenol (NH <sub>2</sub> CHCHOH)	24	Marks et al. (2023)
6	propanal (CH <sub>3</sub> CH <sub>2</sub> CHO)	1-propenol (CH <sub>3</sub> CHCHOH)	42	Singh et al. (2022)
7	acetamide (NH <sub>2</sub> COCH <sub>3</sub> )	1-aminoethenol (NH <sub>2</sub> C(OH)CH <sub>2</sub> )	101	Marks et al. (2023)
8	acetone (CH <sub>3</sub> COCH <sub>3</sub> )	propen-2-ol (CH <sub>3</sub> C(OH)CH <sub>2</sub> )	61	Wang et al. (2023c)
9	hydroxyacetone (CH <sub>3</sub> COCH <sub>2</sub> OH)	prop-1-ene-1,2-diol (CH <sub>3</sub> C(OH)CHOH)	62	Wang et al. (2023b)
		prop-2-ene-1,2-diol (CH <sub>2</sub> C(OH)CH <sub>2</sub> OH)	62	Wang et al. (2023b)
10	methyl acetate (CH <sub>3</sub> COOCH <sub>3</sub> )	1-methoxyethen-1-ol (CH <sub>2</sub> C(OH)OCH <sub>3</sub> )	116	Wang et al. (2023b)
11	3-hydroxypropanal (HCOCH <sub>2</sub> CH <sub>2</sub> OH)	prop-1-ene-1,3-diol (HOCHCHCH <sub>2</sub> OH)	49	Wang et al. (2023b)
12	pyruvic acid (CH <sub>3</sub> COCOOH)	2-hydroxyacrylic acid (CH <sub>2</sub> C(OH)COOH)	28	Kleimeier et al. (2020)

**Note.** The relative energies ( $\Delta E$ ) are relative to their aldehyde or ketone tautomers.

tracers of nonequilibrium chemistry driven by cosmic rays leading to COMs (Abplanalp et al. 2016b; Kleimeier et al. 2021). However, despite the efforts of laboratory simulations, unraveling the formation mechanism of enols within icy grains has just scratched the surface.

In particular, this is true for the C<sub>2</sub>H<sub>2</sub>O<sub>2</sub> isomers including glyoxal (HCOCHO, 1) as well as its enol tautomer hydroxyketene (HOCHCO, 2) and ynol tautomer acetylenediol

(HOCCOH, 3) as potential reactive precursors to larger COMs both in laboratories and the ISM. Glyoxal (1), the simplest  $\alpha$ -dicarbonyl, is a key molecule in atmospheric chemistry (Fu et al. 2008) and serves as a model for investigating the photophysics and photochemistry of small organics (Mielke et al. 2008). Astrophysical models suggest that glyoxal (1) could be formed through recombination of two formyl (HCO) radicals (Woods et al. 2013; Fedoseev et al. 2015;

Butscher et al. 2017; Chuang et al. 2017; Enrique-Romero et al. 2022). Laboratory experiments on carbon monoxide–methane (CO–CH<sub>4</sub>) ices exposed to energetic electrons at 5 K revealed the identification of glyoxal (1) during temperature-programmed desorption (TPD; Abplanalp & Kaiser 2019). Glyoxal (1) has also been detected in the organic residue resulting from a vacuum ultraviolet (VUV)–irradiated ice mixture composed of water (H<sub>2</sub>O), methanol (CH<sub>3</sub>OH), and ammonia (NH<sub>3</sub>; de Marcellus et al. 2015). Therefore, glyoxal (1) is a potential candidate to be searched for in the ISM. Based on Fourier transform infrared (FTIR) spectroscopy and ab initio calculations, Mielke et al. revealed that the irradiation ( $\lambda > 370$  nm) of the glyoxal (1)–methanol complex in solid argon leads to its photoconversion into the hydroxyketene (2)–methanol complex (Mielke et al. 2008), confirming the formation of hydroxyketene (2). Acetylenediol (3), a metastable tautomer of glyoxal (1), is predicted to be 196 kJ mol<sup>-1</sup> less stable at the CCSD(T)/cc-pVTZ level of theory (Vijay & Sastry 2005). It has been prepared and identified in the gas phase by neutralization–reionization mass spectrometry (Terlouw et al. 1986) and detected directly in an argon matrix at 10 K upon irradiation ( $\lambda = 254$  nm) of squaric acid (C<sub>4</sub>H<sub>2</sub>O<sub>4</sub>; Maier & Rohr 1996). The detection of interstellar 1,2-ethenediol (HOCHCHOH; Rivilla et al. 2022) suggests the possible existence of the analogous acetylenediol (3, HOC–COH) derivative in the ISM, in which the carbon–carbon double bond is replaced by a carbon–carbon triple bond (Mó et al. 2023). Acetylenediol (3) is predicted to be formed from glyoxal (1) through keto-enol-ynol tautomerization involving the hydroxyketene (2) as an intermediate (Figure 2; Maier & Rohr 1996). Although this enolization process leading to acetylenediol (3) from glyoxal (1) is unique and interesting in organic chemistry (Maier & Rohr 1996), no experimental evidence has been reported as of now.

Here, we present laboratory experiments on the formation of glyoxal (1) along with its ynol tautomer acetylenediol (3) in low-temperature interstellar model ices comprised of carbon monoxide and water (CO–H<sub>2</sub>O). The ice mixtures were irradiated with energetic electrons, simulating the secondary electrons generated in the track of Galactic cosmic rays (GCRs; Bennett et al. 2011) over lifetimes of molecular clouds of up to 50 million years (Yeghikyan 2011). Utilizing VUV photoionization reflectron time-of-flight mass spectrometry (PI-ReTOF-MS), both glyoxal (1) and acetylenediol (3) were detected in the gas phase via *isomer-specific* photoionization during TPD based on their adiabatic ionization energies (IEs) of C<sub>2</sub>H<sub>2</sub>O<sub>2</sub> isomers (Table 2). These results reveal the formation pathways of glyoxal (1) through radical–radical recombination of formyl radicals and its ynol tautomer acetylenediol (3) via the keto-enol- ynol tautomerization mechanism, advancing the fundamental knowledge of the formation of key reactive organics such as enols in deep space. Water is the most abundant molecule in interstellar ices (Öberg et al. 2011; Tielens 2013), and carbon monoxide is one of the most commonly detected molecules in interstellar ices with a fractional abundance of up to 55% with respect to water toward IRAS 08375–4109 (Thi et al. 2006). Therefore, carbon monoxide and water are suitable choices for simple astrophysical ice analogs. Our results suggest that the hitherto astronomically unobserved glyoxal (1) and acetylenediol (3) represent promising candidates for future astronomical searches via telescopes such as the Atacama Large Millimeter/

submillimeter Array and the James Webb Space Telescope (JWST).

## 2. Experimental

All experiments were carried out in a hydrocarbon-free stainless steel chamber capable of reaching ultrahigh vacuum pressures of a few 10<sup>-11</sup> Torr by magnetically levitated turbomolecular pumps (Jones & Kaiser 2013). A polished silver wafer was mounted on an oxygen-free high-conductivity copper head cooled to 5 K using a closed-cycle helium cryostat (Sumitomo Heavy Industries, RDK-415E). The cold head assembly can rotate within the horizontal plane through a rotatable flange (Thermionics Vacuum Products, RNN-600/FA/MCO) and translate vertically via an adjustable bellows (McAllister, BLT106). The carbon monoxide (CO, 99.99%, Sigma Aldrich) and water (H<sub>2</sub>O, HPLC, Fisher Scientific) vapor were premixed with a ratio of carbon monoxide to water of 1:2. After the silver substrate was cooled to 5 K, the premixed samples were introduced via a glass capillary array to the substrate. Water samples were stored in glass vials and subjected to several freeze–thaw cycles to remove residual atmospheric gases. The ice thickness was monitored via laser interferometry using a helium–neon laser (632.8 nm) during the deposition (Turner et al. 2015). A photodiode was used to record the interference fringes between the reflections of the ice surface and the substrate. Considering the average refractive index ( $n$ ) of  $1.26 \pm 0.04$  between the refractive indices of carbon monoxide ice ( $n = 1.25 \pm 0.03$ ; Pipes et al. 1978; Roux et al. 1980; Bouilloud et al. 2015) and water ice ( $n = 1.27 \pm 0.02$ ; Bouilloud et al. 2015), the thickness of the ice mixture was determined to be  $1000 \pm 200$  nm. FTIR spectra (Thermo Electron, Nicolet 6700) were collected with a resolution of 4 cm<sup>-1</sup> after ice deposition at 5 K. The relative concentration of CO and H<sub>2</sub>O in the ices was determined to be  $(1.4 \pm 0.4)$  utilizing integrated infrared absorptions for  $\nu_1$  (2139 cm<sup>-1</sup>, CO,  $1.12 \times 10^{-17}$  cm molecule<sup>-1</sup>),  $\nu_1$  (2091 cm<sup>-1</sup>, <sup>13</sup>CO,  $1.32 \times 10^{-17}$  cm molecule<sup>-1</sup>),  $2\nu_1$  (4251 cm<sup>-1</sup>, CO,  $1.04 \times 10^{-19}$  cm molecule<sup>-1</sup>) for carbon monoxide, and  $\nu_2$  (1645 cm<sup>-1</sup>, H<sub>2</sub>O,  $9.0 \times 10^{-18}$  cm molecule<sup>-1</sup>),  $\nu_1/\nu_3$  (3700–3000 cm<sup>-1</sup>, H<sub>2</sub>O,  $3.8 \times 10^{-16}$  cm molecule<sup>-1</sup>) for water (Bouilloud et al. 2015; Turner et al. 2018). The ices were then irradiated with 5 keV electrons (SPECS, EQ PU-22) at a current of 50 nA for 120 minutes, resulting in a dose of up to  $15 \pm 3$  eV per molecule of carbon monoxide and  $10 \pm 2$  eV per molecule of water, respectively (Turner et al. 2020). For an interstellar ice grain, these doses correspond to around 50 million years of exposure to GCRs within a molecular cloud (Yeghikyan 2011). Utilizing Monte Carlo simulations carried out in the CASINO program (Drouin et al. 2007), the average penetration depth of the electrons was  $360 \pm 60$  nm; 99% of the electron energy was deposited in the top  $600 \pm 50$  nm sample layers, which is less than the ice thickness, to prevent the interaction between the electrons and the substrate (Turner et al. 2021).

After the irradiation, the ices were heated to 300 K at 1 K minute<sup>-1</sup> using a TPD scheme. During TPD, subliming molecules were photoionized in the gas phase by pulsed 30 Hz coherent VUV light at photon energies of 10.82, 9.75, 9.10, 8.81, and 8.20 eV. VUV light was generated via a two-photon resonant difference four-wave mixing ( $\omega_{\text{vuv}} = 2\omega_1 - \omega_2$ ) scheme using krypton or xenon gases as a nonlinear medium. Detailed parameters for VUV generation are listed in Table 3. The VUV photons were separated from other energy photons via a lithium fluoride biconvex lens (Korth Kristalle, R1 = R2 = 131 mm) in an off-axis geometry and passed  $2.0 \pm 0.5$  mm above the ice

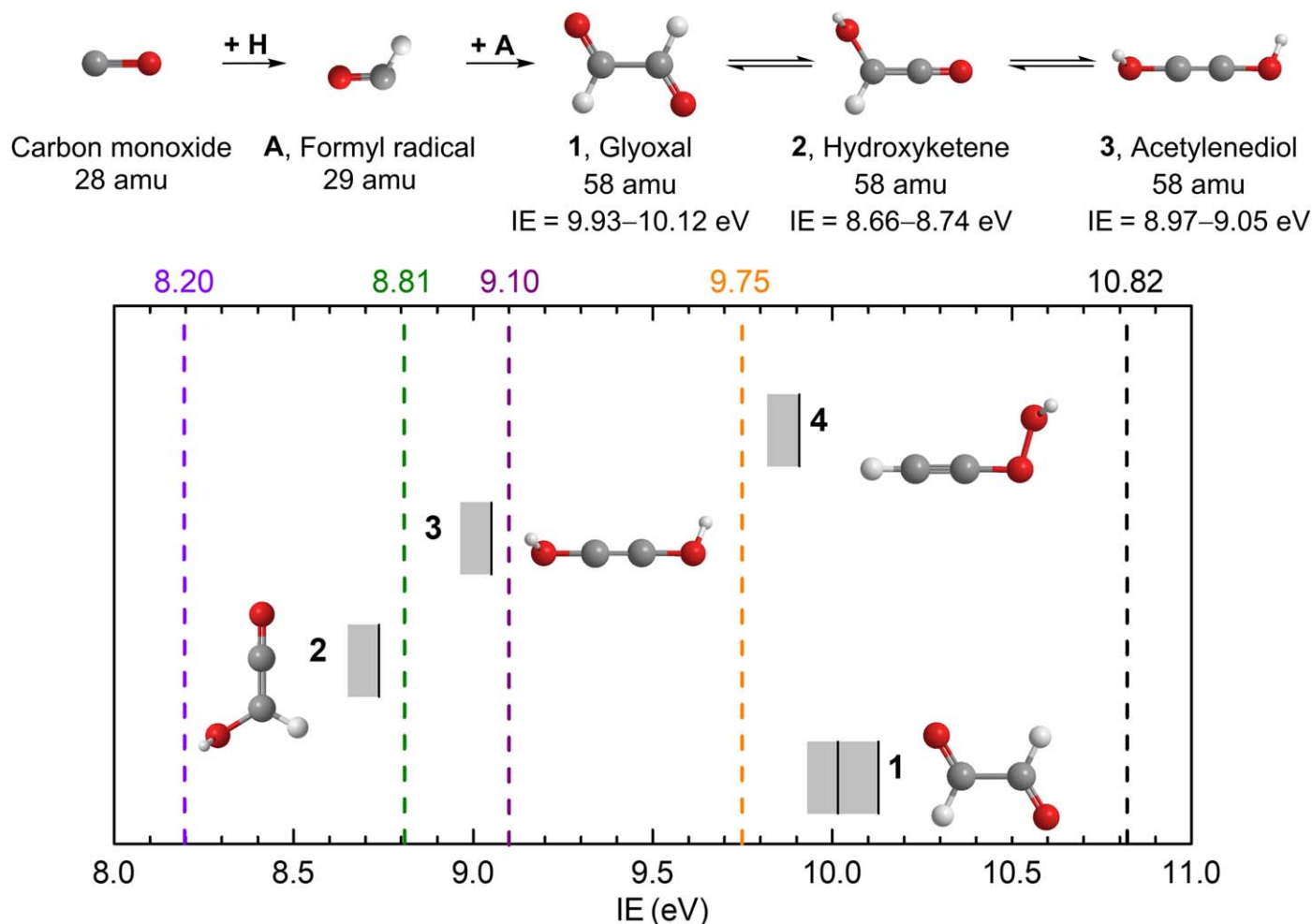


**Figure 2.** Reaction scheme leading to  $C_2H_2O_2$  ( $m/z = 58$ ) isomers (1–3) in irradiated carbon monoxide–water ices (top). Barrierless reactions of two formyl radicals ( $H\dot{C}O$ , A) produce 1; tautomerization of 1 leads to isomers 2 and 3. The adiabatic ionization energies (IEs) are corrected for computational accuracy at the CCSD(T)-F12b/cc-pVTZ-F12 level of theory (Table 2). The bottom figure compiles the computed IEs of  $C_2H_2O_2$  isomers (black solid lines) and IE ranges (gray area) after error analysis. Five VUV photon energies (dashed lines) were selected to photoionize subliming molecules during TPD.

**Table 2**

Error Analysis of Adiabatic Ionization Energies (IEs) and Relative Energies ( $\Delta E$ ) of Distinct  $C_2H_2O_2$  Isomers 1–4; IEs and  $\Delta E$  Were Computed at the CCSD(T)-F12b/cc-pVTZ-F12 Level of Theory Including the Zero-point Vibrational Energy (ZPVE) Corrections

Name	Isomer	$\Delta E$ ( $\text{kJ mol}^{-1}$ )	Computed IE (eV)	Corrected IE Ranges (eV)
Glyoxal	<i>anti</i> -1	0	10.12	10.04–10.12
	<i>syn</i> -1	19	10.01	9.93–10.01
Hydroxyketene	2	65	8.74	8.66–8.74
Acetylenediol	3	193	9.05	8.97–9.05
Ethynyl hydroperoxide	4	407	9.90	9.82–9.90

**Note.** The IE ranges are corrected for the thermal and Stark effect by  $-0.03$  eV and the combined error limits of  $-0.05/+0.03$  eV (Zhu et al. 2022a).

surface to ionize subliming species in the gas phase. The resulting ions were detected via a reflectron time-of-flight mass spectrometer (Jordan TOF Products, Inc.). Ion signals were amplified by a preamplifier (Ortec 9305) and recorded by a

multichannel scaler (FAST ComTec, MCS6A). The accumulation time for each recorded mass spectra during TPD was 2 minutes (3600 sweeps). To confirm the mass assignments, isotopically labeled experiments were performed using  $^{13}C$ CO (99% atom  $^{13}C$ , Sigma Aldrich),  $^{13}C^{18}O$  (95% atom  $^{18}O$ , 99% atom  $^{13}C$ , Sigma Aldrich),  $D_2O$  (99.9% atom D, Sigma Aldrich), and  $H_2^{18}O$  (99%  $^{18}O$ , Sigma Aldrich). An additional blank experiment was performed without electron irradiation, verifying that the observed ion signals at mass-to-charge ratio ( $m/z$ ) of 58 were caused by an external energy source.

### 3. Theoretical

All computations make use of coupled cluster singles, doubles, and perturbative triples within the explicitly correlated formalism [CCSD(T)-F12b] with the cc-pVTZ-F12 basis set as available in MOLPRO 2022.3 (Adler et al. 2007; Peterson et al. 2008; Yousaf & Peterson 2008; Knizia et al. 2009; Werner et al. 2021). Harmonic frequencies confirm the structures as minima and produce the zero-point vibrational energies (ZPVEs), which are added to the total electronic energies. Differences in the electronic plus ZPVE energies between conformers produce the relative energies, and differences between these energies for the neutral and radical

**Table 3**  
Difference Four-wave Mixing Parameters for the Generation of VUV Light with an Uncertainty Less than 0.001 eV for Photon Energies

VUV Photon Energy ( $2\omega_1 - \omega_2$ ) (eV)	Nonlinear Medium	$\omega_1$ Laser Wavelength (nm)	$\omega_1$ Dye	$\omega_2$ Laser Wavelength (nm)	$\omega_2$ Dye
10.82	Krypton	202.316	Rhodamine 610 and 640	863.117	LDS 867
9.75	Krypton	202.316	Rhodamine 610 and 640	494.657	Coumarin 503
9.10	Xenon	222.566	Coumarin 450	607.379	Rhodamine 610 and 640
8.81	Xenon	222.566	Coumarin 450	532	...
8.20	Xenon	249.628	Coumarin 503	715.207	LDS 722

cation produce the IEs. The same procedure is utilized to compute degradation products where the final energies are simple Hess's Law reaction energetics based upon the computed electronic plus ZPVE energies. Electronic energies, optimized Cartesian coordinates, and harmonic frequencies are provided in the [Appendix](#), Table A1.

## 4. Results and Discussion

### 4.1. Infrared Spectroscopy

FTIR spectra of carbon monoxide–water (CO–H<sub>2</sub>O) ices were collected before, during, and after the irradiation with energetic electrons (Figure 3). Before the irradiation, the CO–H<sub>2</sub>O ice spectra are dominated by the CO stretching (CO, 2139 cm<sup>-1</sup>; <sup>13</sup>CO, 2092 cm<sup>-1</sup>) and overtone (4251 cm<sup>-1</sup>) modes of carbon monoxide, OH dangling (3630 cm<sup>-1</sup>), OH stretching ( $\nu_1/\nu_3$ , 3000–3610 cm<sup>-1</sup>), and H–O–H bending ( $\nu_2$ , 1644 cm<sup>-1</sup>) modes for water (Bouilloud et al. 2015). Processing of the CO–H<sub>2</sub>O ice resulted in several new absorptions. The absorptions at 2345 and 2279 cm<sup>-1</sup> were assigned to C=O stretching ( $\nu_3$ ) of carbon dioxide (Bouilloud et al. 2015), which is the dominant product in processed CO-containing ices (Abplanalp & Kaiser 2019; Schmidt et al. 2019). Formaldehyde (H<sub>2</sub>CO) was identified with the C=O stretching ( $\nu_2$ , 1716 cm<sup>-1</sup>) and CH<sub>2</sub> scissoring ( $\nu_3$ , 1499 cm<sup>-1</sup>) modes (Bouilloud et al. 2015). The absorption at 1849 cm<sup>-1</sup> can be linked to the  $\nu_3$  fundamental (CO stretch) of the formyl radical (HCO; Milligan & Jacox 1964), which has been identified previously in CO-containing interstellar analog ices such as CO–H<sub>2</sub>S (1840 cm<sup>-1</sup>; Wang et al. 2022), CO–C<sub>2</sub>H<sub>2</sub> ice (1853 cm<sup>-1</sup>; Abplanalp & Kaiser 2019), CO–CH<sub>4</sub> ice (1853 cm<sup>-1</sup>; Bennett et al. 2005), and CO–CH<sub>3</sub>OH ice (1843 cm<sup>-1</sup>; Bennett & Kaiser 2007). The absorptions of carbon dioxide, formaldehyde, and formyl have been shifted in isotopically labeled systems (<sup>13</sup>CO–H<sub>2</sub>O ice, CO–D<sub>2</sub>O ice, and <sup>13</sup>C<sup>18</sup>O–H<sub>2</sub><sup>18</sup>O ice), as shown in Figure A1. It is worth noting that the absorption at 1716 cm<sup>-1</sup> may also be linked to the C=O stretching of glyoxal (1) (Verderame et al. 1970; Hudson et al. 2005). The OH stretching (3586 cm<sup>-1</sup>) and OH bending (1212 cm<sup>-1</sup>) modes of acetylenediol (3) have been observed in an argon matrix at 10 K previously (Maier & Rohr 1996); however, they were not detected in the irradiated H<sub>2</sub>O–CO ice due to the overlap of functional groups such as hydroxyl group (–OH) or the low sensitivity of our FTIR setup. Therefore, an isomer-selective identification of the target isomers 1–3 cannot be accomplished by infrared spectroscopy; an alternative, more sensitive approach is required to identify individual C<sub>2</sub>H<sub>2</sub>O<sub>2</sub> isomers formed in these ices.

### 4.2. PI-ReTOF-MS

PI-ReTOF-MS was utilized to identify individual C<sub>2</sub>H<sub>2</sub>O<sub>2</sub> isomers during the heating of the irradiated ices. This technique allows for the identification of specific structural isomers based on their distinct desorption temperatures and adiabatic IEs (Turner & Kaiser 2020). Here, the subliming products were photoionized in separate experiments with photon energies of 10.82, 9.75, 9.10, 8.81, and 8.20 eV to determine which C<sub>2</sub>H<sub>2</sub>O<sub>2</sub> isomers were formed (Figure 2). Photons with energies of 10.82 eV can ionize all isomers glyoxal (1), hydroxyketene (2), acetylenediol (3), and ethynyl hydroperoxide (4). 9.75 and 9.10 eV photons can ionize hydroxyketene (2, IE = 8.66–8.74 eV) and acetylenediol (3, IE = 8.97–9.05 eV), whereas 8.81 eV photons can only ionize hydroxyketene (2). 8.20 eV photons cannot ionize either C<sub>2</sub>H<sub>2</sub>O<sub>2</sub> isomer. At a photon energy of 10.82 eV, the TPD profile of  $m/z = 58$  in the irradiated CO–H<sub>2</sub>O ice shows a broad sublimation event that starts at 140 K and ends at 185 K (Figure 4; Turner et al. 2021). After the early sublimation event, a shoulder peaking at around 170 K is found with varying intensity in isotopically labeled ices. This is attributed to the sublimation of molecules trapped within the water-ice matrix that comprises the bulk of the ice until its sublimation. Since the ion signal of  $m/z = 58$  can be associated with C<sub>2</sub>H<sub>2</sub>O<sub>2</sub>, C<sub>3</sub>H<sub>6</sub>O, and/or C<sub>4</sub>H<sub>10</sub>, it is imperative to confirm the assignment of the molecular formula using isotopically labeled precursors. In particular, this TPD profile shifts by 2 atomic mass unit (amu) from  $m/z = 58$  to  $m/z = 60$  in both <sup>13</sup>CO–H<sub>2</sub>O and CO–D<sub>2</sub>O ices indicating the presence of two carbon atoms and two deuterium atoms, respectively. Furthermore, the replacement of the CO–H<sub>2</sub>O ice by <sup>13</sup>C<sup>18</sup>O–H<sub>2</sub><sup>18</sup>O ice shifts the  $m/z$  by 6 amu from  $m/z = 58$  (C<sub>2</sub>H<sub>2</sub>O<sub>2</sub><sup>+</sup>) to  $m/z = 64$  (<sup>13</sup>C<sub>2</sub>H<sub>2</sub><sup>18</sup>O<sub>2</sub><sup>+</sup>), indicating the presence of two carbon atoms and two oxygen atoms. In addition, the formation of C<sub>3</sub>H<sub>6</sub>O isomers can be ruled out from the TPD profiles of isotopically labeled ice mixtures (Figure A2). Hence, the ion signal of  $m/z = 58$ , at least in the range from 140 to 170 K, can be clearly linked to a molecule of the formula C<sub>2</sub>H<sub>2</sub>O<sub>2</sub>.

Since the 10.82 eV photons are capable of ionizing all C<sub>2</sub>H<sub>2</sub>O<sub>2</sub> isomers, the TPD profile of  $m/z = 58$  can be linked to isomers 1–4. This profile is deconvoluted with three Gaussian fits peaking at 156 K (peak 1), 161 K (peak 2), and 169 K (peak 3), respectively (Figure 5(a)). It should be noted that these peaks are not present in the blank experiment conducted under the same conditions but without exposing the ices to ionizing radiation, confirming that the sublimation event of  $m/z = 58$  (C<sub>2</sub>H<sub>2</sub>O<sub>2</sub><sup>+</sup>) is the result of the irradiation exposure of the ices. Utilizing a photon energy of 9.75 and 9.10 eV, at which glyoxal (1, IE = 9.93–10.12 eV) and ethynyl hydroperoxide

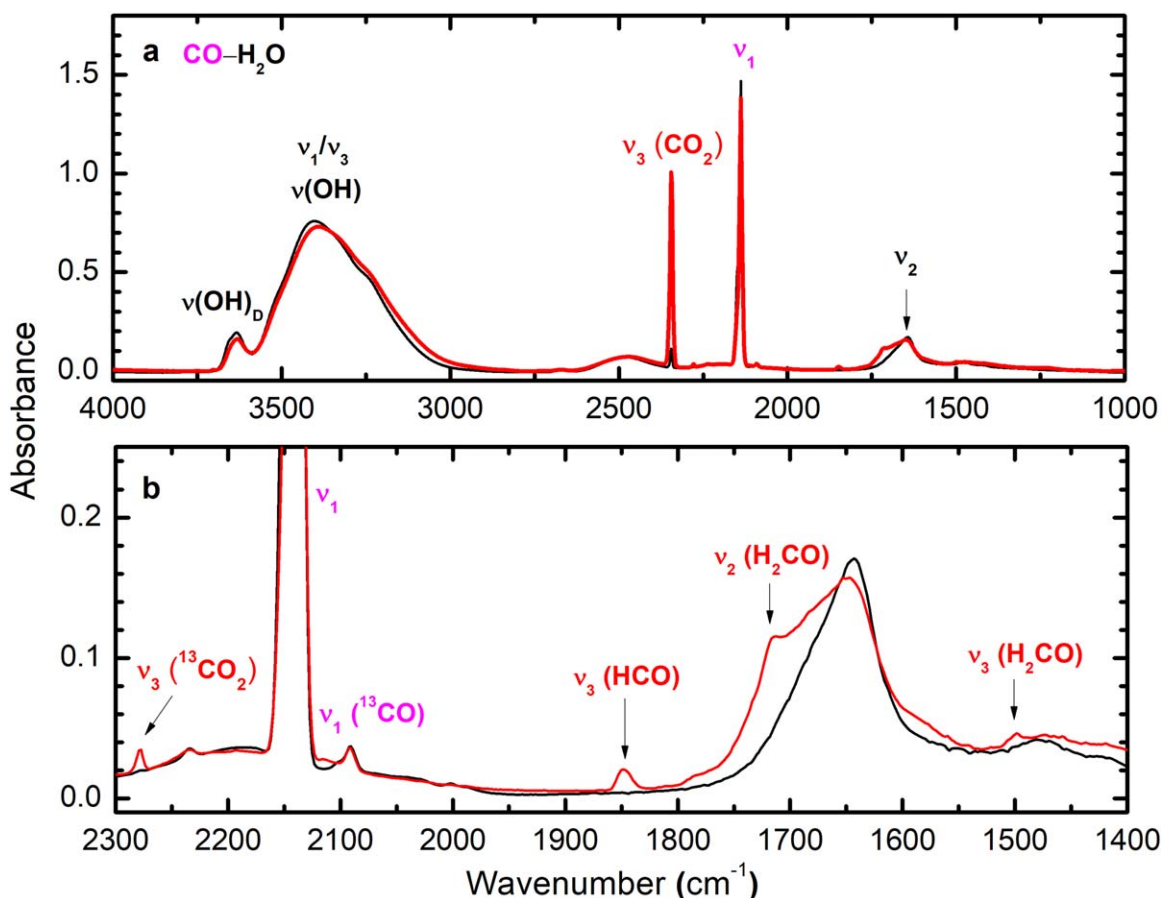


**Figure 3.** FTIR spectra of CO–H<sub>2</sub>O ice at 5 K before (black line) and after (red line) irradiation. A magnified view of the region between 2300 and 1400 cm<sup>-1</sup> shows new peaks after irradiation.

(4, IE = 9.82–9.90 eV) cannot be ionized, the early sublimation event (peak 1) vanishes (Figure 5(b)), indicating that peak 1 is associated with glyoxal (1) and/or ethynyl hydroperoxide (4). We calculated the dissociation pathways for the cation of ethynyl hydroperoxide (4) at the CCSD(T)-F12b/cc-pVTZ-F12 level of theory (Figure 6); cleaving the O–O bond in the cation is strictly Morse-like behavior and only requires 20 kJ mol<sup>-1</sup> (pathway a). After the photoionization at 10.82 eV, the excess energy in the cation is at least 89 kJ mol<sup>-1</sup>, which is notably larger than the energy needed to open the dissociation pathway in which the cation (HCCOOH<sup>+</sup>) leads to fragment ion HCCO<sup>+</sup> plus hydroxyl radical ( $\dot{\text{O}}\text{H}$ ) (Figure 6). One would expect to observe an ion signal of HCCO<sup>+</sup> ( $m/z = 41$ ) at 10.82 eV if ethynyl hydroperoxide (4) was formed; however, no ion signal was detected at  $m/z = 41$ , ruling out the formation of ethynyl hydroperoxide (4) under current experimental conditions. Therefore, peak 1 is assigned to glyoxal (1). It is worth noting that glyoxal (1) is known to desorb near 160 K (Butscher et al. 2017), which agrees well with our results.

Additionally, the TPD profile of  $m/z = 58$  recorded at both 9.75 and 9.10 eV exhibits a sublimation event corresponding to peaks 2 and 3, which can be linked to hydroxyketene (2, IE = 8.66–8.74 eV) and/or acetylenediol (3, IE = 8.97–9.05 eV). We then lowered the photon energy to 8.81 eV, at which only hydroxyketene (2) can be ionized. In contrast to the results at 9.75 eV, peak 2 vanishes at 8.81 eV (Figure 5(b)), suggesting that this event can be linked to acetylenediol (3). At 8.81 eV, a sublimation event (peak 3) remains. Previous work revealed that

water has a sublimation event peaking at 170 K (Zheng et al. 2006) and 165 K (Bennett et al. 2011) in electron-irradiated H<sub>2</sub>O ice and CO–H<sub>2</sub>O ice, respectively. The coincidence of peak 3 at 169 K can be due to the cosublimation of a compound with water molecules. In addition, the sublimation event of  $m/z = 72$  that can be assigned to C<sub>3</sub>H<sub>4</sub>O<sub>2</sub> isomers (Turner et al. 2021) partially matches the TPD profile of  $m/z = 58$  (Figure A3), indicating that peak 3 may originate from the fragment of the dissociative photoionization of C<sub>3</sub>H<sub>4</sub>O<sub>2</sub> species. Therefore, peak 3 cannot be uniquely assigned to hydroxyketene (2). Further lowering the photon energy to 8.20 eV eliminates peak 3, and no ion signal of  $m/z = 58$  was observed. Overall, the PI-ReTOF-MS studies demonstrate the gas-phase detection of glyoxal (1) and acetylenediol (3), and a tentative identification of hydroxyketene (2). The detected counts of glyoxal (1) and acetylenediol (3) in the irradiated CO–H<sub>2</sub>O ices were  $1800 \pm 200$  and  $880 \pm 100$  counts, respectively.

Having provided evidence for the formation of glyoxal (1) and acetylenediol (3) in carbon monoxide–water ices under astrophysical conditions, we shift our attention to their potential formation pathways. *First*, upon the interaction of energetic electrons, a water molecule undergoes unimolecular decomposition to form a hydroxyl radical ( $\dot{\text{O}}\text{H}$ ) and a suprathermal hydrogen atom ( $\dot{\text{H}}$ ) with excess kinetic energy of up to a few eV (reaction in Equation (1); Zheng et al. 2006). Since the reaction in Equation (1) is strongly endoergic by 466 kJ mol<sup>-1</sup> (Bennett et al. 2011), the input of energy originating from GCRs is necessary. *Second*, the addition of the hydrogen atom

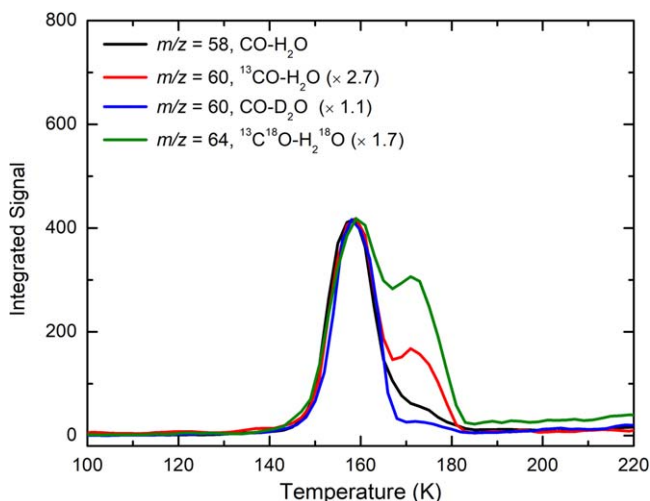
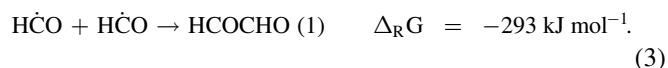
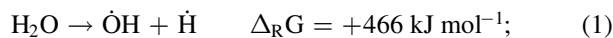


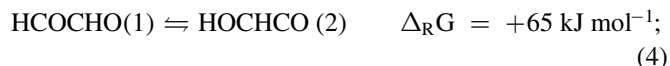
**Figure 4.** TPD profiles recorded at 10.82 eV for isotopically labeled carbon monoxide–water ice mixtures:  $m/z = 58$  in irradiated CO–H<sub>2</sub>O ice,  $m/z = 60$  in irradiated <sup>13</sup>CO–H<sub>2</sub>O ice,  $m/z = 60$  in irradiated CO–D<sub>2</sub>O ice, and  $m/z = 64$  in irradiated <sup>13</sup>C<sup>18</sup>O–H<sub>2</sub><sup>18</sup>O ice.

to a carbon monoxide molecule leads to the formation of the formyl radical (HĊO) via the reaction in Equation (2) (Wang et al. 2022). This reaction is exoergic by 60 kJ mol<sup>-1</sup> with an entrance barrier of 11 kJ mol<sup>-1</sup> (Bennett et al. 2005), which can be overcome by the excess kinetic energy of the suprathreshold hydrogen atom. Extensive studies have demonstrated the formation of the formyl radical (HĊO) in CO–H<sub>2</sub>O ice analogs under simulated astrophysical conditions, which involve reactions initiated by energetic heavy ions (46 MeV <sup>58</sup>Ni<sup>11+</sup>; de Barros et al. 2022), protons (0.8 MeV; Hudson & Moore 1999), electrons (5 keV; Bennett et al. 2011; Eckhardt et al. 2019; Turner et al. 2020, 2021), X-rays (Jiménez-Escobar et al. 2016), and VUV photolysis (Milligan & Jacox 1971). This is also confirmed by our FTIR results that the CO stretch (1849 cm<sup>-1</sup>) of formyl radical was observed in irradiated CO–H<sub>2</sub>O ice. *Third*, if the formyl radical has a favorable recombination geometry with another nearby formyl radical, the barrierless radical–radical recombination of two formyl radicals can proceed to form glyoxal (1) via the reaction in Equation (3). It is worth noting that the reaction in Equation (3) has a diffusion barrier of around 4 kJ mol<sup>-1</sup> on a water ice surface calculated at the BHLYP-D3(BJ)/6-311++G(2df,2pd) level of theory (Enrique-Romero et al. 2022). The origin of the barrier is that formyl radicals need to overcome partly the intermolecular forces with the surfaces to orient and react (Enrique-Romero et al. 2022). This small barrier can be easily overcome by the energy contributed by energetic electrons. Glyoxal (1) exists in stable planar *syn* conformation and *anti* conformation that refer to the relative positions of the two oxygen atoms with respect to the carbon–carbon single bond. The *antiglyoxal* is more stable than the *syn* form by 19 kJ mol<sup>-1</sup> (Table 2), indicating that the *anti* conformation is predominantly at 300 K equilibrium (Mielke et al. 2008). The isomerization barrier from *antiglyoxal* to *synglyoxal* is 23 kJ mol<sup>-1</sup> (Koch et al. 2001; Xiong et al. 2014). The formation of an *antiglyoxal* via the reaction in Equation (3) is exoergic by 293 kJ mol<sup>-1</sup> calculated at the M06-2X-D3/aug-cc-pVTZ level of theory (Butscher et al. 2017). Previous studies on the dimerization of formyl radical in the gas

phase (Clark et al. 1978) and rare gas matrix (Butscher et al. 2017) indicate that the production of formaldehyde is the favored pathway. This route may contribute to the formation of formaldehyde in the irradiated ices (Butscher et al. 2015) as formaldehyde was observed in our FTIR spectra. However, the presence of neighboring molecules with similar vibrational structures in the ices may aid an intermolecular energy transfer (Wang et al. 2023a), and effectively stabilize glyoxal (1) formed via highly exoergic recombination. Furthermore, cage effects can impose a significant barrier to dissociative reaction pathways such as that which produces formaldehyde.



Finally, glyoxal (1) likely undergoes subsequent keto-enol tautomerization to form hydroxyketene (2) and acetylenediol (3). Glyoxal (1) has a pair of conjugated carbon–oxygen double bonds; it can first tautomerize to hydroxyketene (2) through the reaction in Equation (4) (Mielke et al. 2008), which can further tautomerize to acetylenediol (3) via reaction (5) (Maier & Rohr 1996). The reactions in Equations (4) and (5) are endoergic by 65 and 128 kJ mol<sup>-1</sup>, respectively. The reaction in Equation (4) involves a four-member-ring transition state with a reaction barrier of 318 kJ mol<sup>-1</sup> calculated at the WIU level of theory (Xiong et al. 2014). The barrier of the reaction in Equation (5) was predicted to be 373 kJ mol<sup>-1</sup> at the MP2/6-31G\*\*//HF/6-31G\*\* level of theory (Lewars & Bonnycastle 1997). These tautomerization barriers can be overcome by the energy contributed by GCRs (Wang et al. 2022).



## 5. Astrophysical Implications

This work presents laboratory experiments on the formation of hitherto astronomically unobserved glyoxal (1) along with its enol tautomer acetylenediol (3) in interstellar model ices composed of carbon monoxide and water. Prior studies on chemical modeling of interstellar ices suggest that glyoxal (1) could be formed through radical–radical recombination of formyl radicals (HĊO; Woods et al. 2013; de Marcellus et al. 2015; Fedoseev et al. 2015; Maity et al. 2015; Abplanalp et al. 2016a; Butscher et al. 2017; Chuang et al. 2017; Abplanalp & Kaiser 2019; Kleimeier et al. 2021; Turner et al. 2021). The formyl radical is one of the most well-known astrophysically relevant radical species (Butscher et al. 2017) and has been detected in the Galactic molecular clouds W3, NGC 2024, W51, and K3-50 (Snyder et al. 1976), the cold and dense core B1-b (Cernicharo et al. 2012), the Blazars BL Lacertae objects and 3C 111 (Liszt et al. 2014), prestellar cores (Bacmann & Faure 2016), and the solar-type protostellar binary IRAS 16 293–2422 (Rivilla et al. 2019). Although *synglyoxal* (1) may be detected in the ISM due to its large dipole moment (4.3 D; Leroux et al. 2020), glyoxal (1) would be in its preferred *anti* configuration with a zero dipole moment by symmetry,

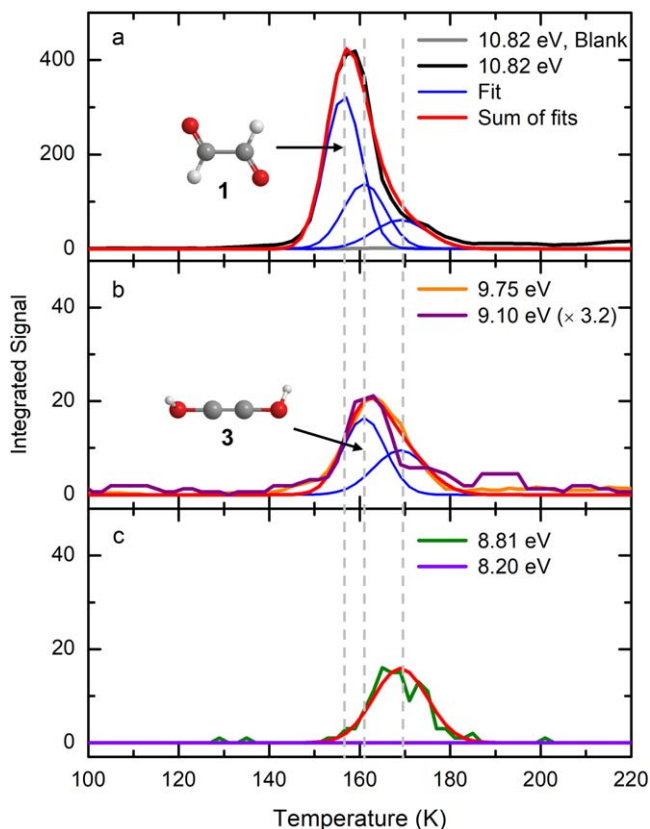


**Figure 5.** TPD profiles for  $m/z = 58$  ( $\text{C}_2\text{H}_2\text{O}_2^+$ ) in irradiated CO–H<sub>2</sub>O ice recorded at 10.82, 9.75, 9.10, 8.81, and 8.20 eV, as well as in the blank (unirradiated) experiment recorded at 10.82 eV. The solid red lines indicate the total fits of the spectra.

which makes its astronomical detection difficult (Leroux et al. 2021). Once formed in the ices, glyoxal (1) may further lead to the formation of formaldehyde and carbon monoxide (Butscher et al. 2017). Further, glyoxal (1) and acetylenediol (3) may be found with low concentrations in the ISM due to their high reactivity.

As of now, the enols vinyl alcohol ( $\text{CH}_2\text{CHOH}$ ), 1,2-ethenediol ( $\text{HOCHCHOH}$ ), and 3-hydroxypropenal ( $\text{HOCHCHCHO}$ ; tentative) have been detected toward the dense molecular cloud Sagittarius B2(N) (Turner & Apponi 2001), the G +0.693–0.027 molecular cloud (Rivilla et al. 2022), and the solar-type protostar IRAS 16293–2422 (Coutens et al. 2022), respectively. Laboratory simulations suggested that both vinyl alcohol and 1,2-ethenediol can be formed through the enolization of their aldehydes (Abplanalp et al. 2016b; Kleimeier & Kaiser 2021; Kleimeier et al. 2021; Zhu et al. 2022b). Our findings reveal the formation route of ynol acetylenediol (3) via keto-enol-ynol tautomerization of glyoxal (1) with enol hydroxyketene (2) as an intermediate, which was tentatively identified in our experiments. These pathways may occur via GCR-induced keto-enol tautomerization reactions in carbon monoxide-rich and water-rich interstellar ices. Although acetylenediol (3) has been detected in argon matrix isolation (Maier & Rohr 1996), we present its first identification in interstellar ice analogs. The observation of acetylenediol (3) reveals that keto-enol-ynol tautomerization can proceed in interstellar ices composed of simple, abundant precursors such as carbon monoxide and water, advancing our fundamental knowledge

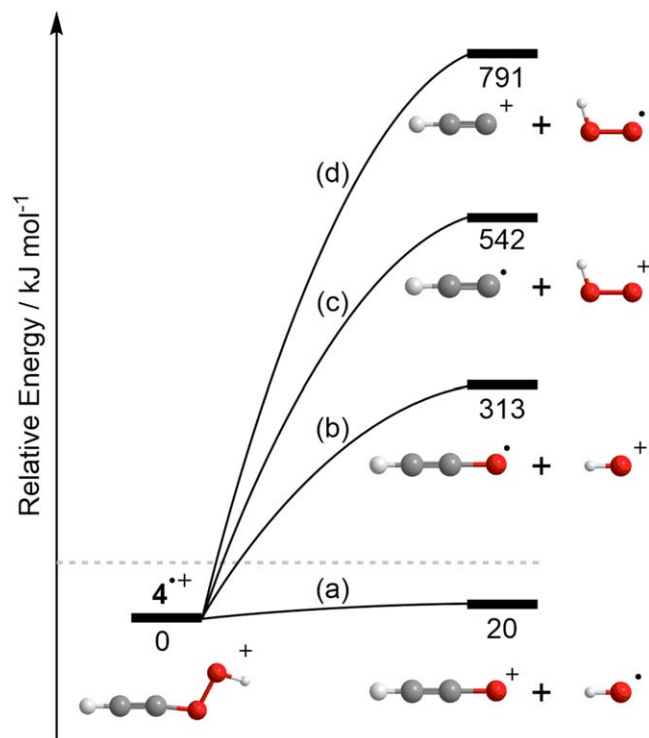


**Figure 6.** Calculated dissociation pathways of the ethynyl hydroperoxide radical cation ( $4^+$ ). The energies ( $\text{kJ mol}^{-1}$ ) computed at the CCSD(T)-F12b/cc-pVTZ-F12 level are relative to the cation  $4^+$ . The dashed gray line indicates the excess internal energy ( $89 \text{ kJ mol}^{-1}$ ) in the cation after photoionization at 10.82 eV.

of the formation mechanisms of key reactive COMs such as enols in deep space.

Water is the most abundant molecule in interstellar ices (Öberg et al. 2011; Tielens 2013), and carbon monoxide has been detected at levels up to 55% relative to water toward IRAS 08375–4109 (Thi et al. 2006). Considering the abundance of carbon monoxide and water in the interstellar ices, both glyoxal (1) and acetylenediol (3) are promising candidates to search for toward background stars such as Taurus field star Elias 16 (Chiar et al. 1995), NIR38, and J110621 (McClure et al. 2023); and young stellar objects such as IRAS 08375–4109 (Thi et al. 2006), NGC 7538 IRS 9 (Whittet 1997), GL 7009S, and W33A (Gibb et al. 2000). The high-resolution FTIR spectra of glyoxal (1,  $\text{C}_2\text{H}_2\text{O}_2$ ; Larsen et al. 2002) as well as its isotopomers (Larsen et al. 2003) are known. Although the rotational spectrum of acetylenediol (3) is lacking, two IR bands at  $3586$  and  $1212 \text{ cm}^{-1}$  have been observed in an argon matrix (Maier & Rohr 1996). Glyoxal (1) and acetylenediol (3) may act as reactive precursors to form biorelevant molecules. Through successive hydrogenation, glyoxal (1) can convert to the sugar-related glycolaldehyde ( $\text{HOCH}_2\text{CHO}$ ) and ethylene glycol ( $\text{HOCH}_2\text{CH}_2\text{OH}$ ), which have been detected toward the Galactic Center source Sagittarius B2(N) (Hollis et al. 2000, 2002). Once formed in interstellar ices, these molecules may eventually be incorporated into comets and delivered to planets like early Earth. In fact, extraterrestrial  $\text{C}_2\text{H}_2\text{O}_2$  species have recently been detected and can likely be assigned to glyoxal (1) in comet 67P’s dusty coma (Hänni et al. 2023). A firm detection of glyoxal (1) and acetylenediol (3) in the ISM in conjunction

with their reaction pathways leading to other organics could enhance our comprehension of how high-energy tautomers contribute to the formation mechanisms of COMs in deep space (Kleimeier & Kaiser 2022).

### Acknowledgments

The Hawaii group acknowledges support from the US National Science Foundation, Division of Astronomical Sciences under grant AST-2103269. R.C.F. is thankful for the support from NASA grants NNX22ZHA004C and NNX17AH15G, startup funds provided by the University of Mississippi, and computational support from the Mississippi Center for Supercomputing Research funded in part by NSF grants CHE-1338056 and OIA-1757220.

### Conflicts of Interest

The authors declare no competing financial interests.

### Appendix

Magnified view of FTIR spectra for isotopically labeled carbon monoxide–water ices before and after irradiation is presented in Figure A1. TPD profiles recorded at 10.82 eV for isotopically labeled ice mixtures are shown in Figure A2, ruling out the formation of  $C_3H_6O$  isomers. TPD profiles of  $m/z = 58$  and  $m/z = 72$  in irradiated CO–H<sub>2</sub>O ices recorded at 8.81 eV are provided in Figure A3. Electronic energies, optimized Cartesian coordinates, and vibrational frequencies of  $C_2H_2O_2$  isomers calculated at the CCSD(T)-F12b/cc-pVTZ-F12 level of theory are shown in Table A1.

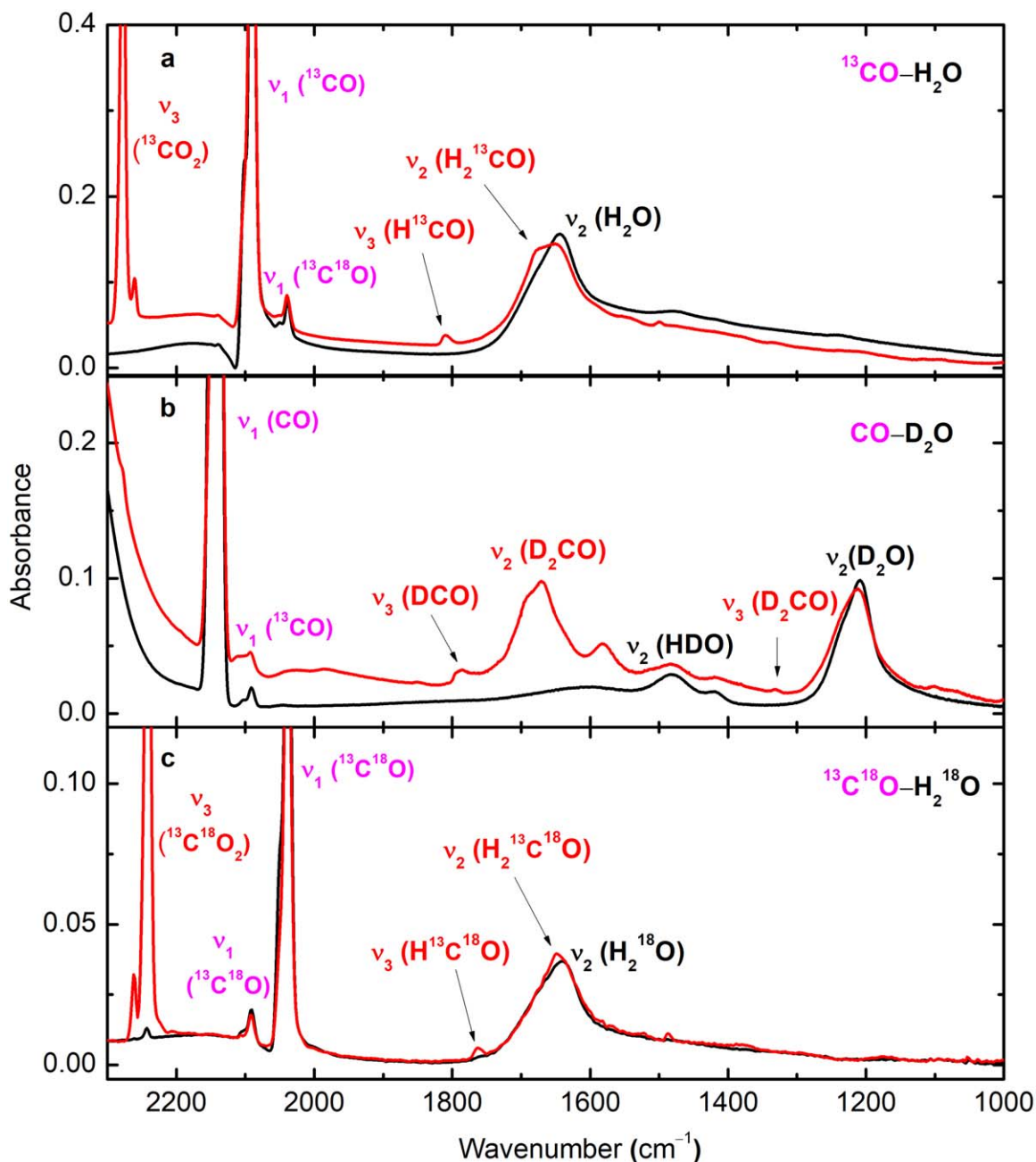


**Figure A1.** Magnified view of FTIR spectra of  $^{13}CO$ –H<sub>2</sub>O ice (a), CO–D<sub>2</sub>O ice (b), and  $^{13}C^{18}O$ –H<sub>2</sub><sup>18</sup>O ice (c) before (black line) and after (red line) irradiation.

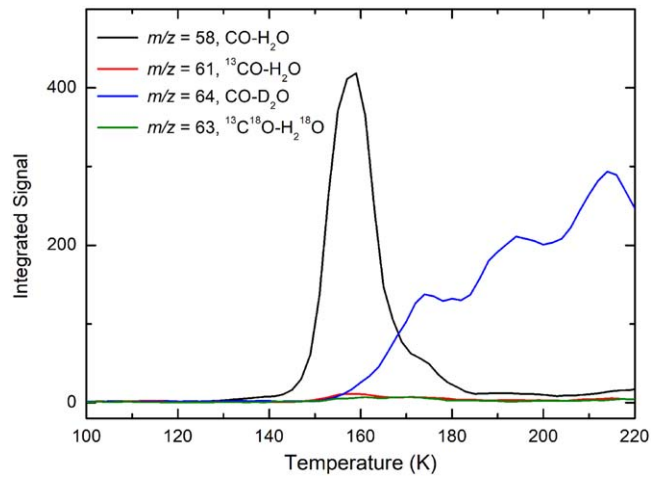


**Figure A2.** TPD profiles recorded at 10.82 eV for isotopically labeled carbon monoxide–water ice mixtures ( $m/z = 58$  in irradiated CO–H<sub>2</sub>O ice,  $m/z = 61$  in irradiated <sup>13</sup>CO–H<sub>2</sub>O ice,  $m/z = 64$  in irradiated CO–D<sub>2</sub>O ice, and  $m/z = 63$  in irradiated <sup>13</sup>C<sup>18</sup>O–H<sub>2</sub><sup>18</sup>O ice), ruling out the formation of C<sub>3</sub>H<sub>6</sub>O isomers.

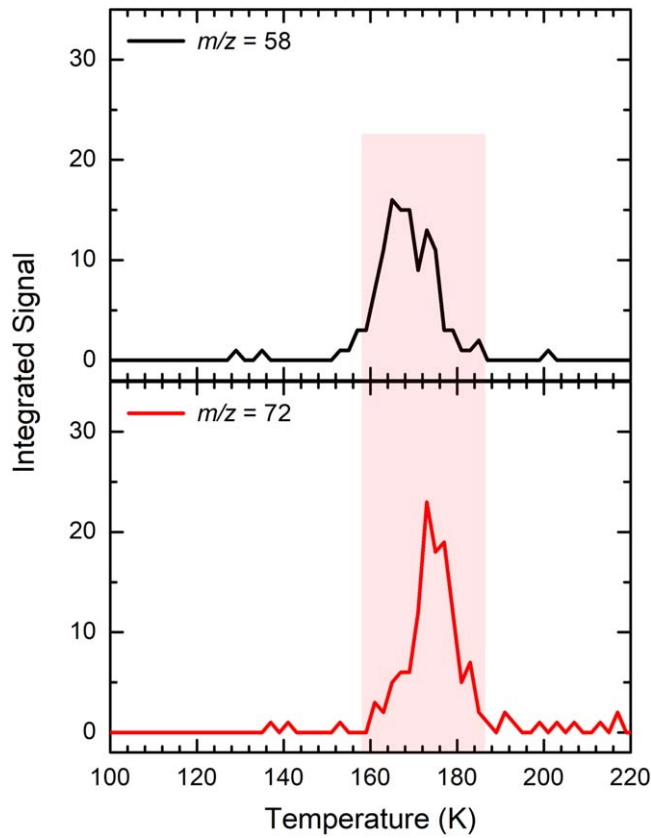


**Figure A3.** TPD profiles of  $m/z = 58$  (C<sub>2</sub>H<sub>2</sub>O<sub>2</sub><sup>+</sup>) and  $m/z = 72$  (C<sub>3</sub>H<sub>4</sub>O<sub>2</sub><sup>+</sup>) in the irradiated CO–H<sub>2</sub>O ices recorded at a photon energy of 8.81 eV. The red-shaded region indicates their overlap in sublimation temperatures.

**Table A1**Electronic Energy (Hartree;  $E$  at 0 K), Optimized Cartesian Coordinates ( $\text{\AA}$ ), and Vibrational Frequencies ( $\text{cm}^{-1}$ ) of  $\text{C}_2\text{H}_2\text{O}_2$  Isomers Computed at the CCSD(T)-F12b/cc-pVTZ-F12 Level of Theory

Isomer	Cartesian Coordinates				Frequency	
	Atom	$(\text{\AA})$			$(\text{cm}^{-1})$	
		X	Y	Z		
<i>anti</i> -1 $E = -227.5816$ ZPVE = 0.03697535 $E$ (total) = -227.54462	C	-0.643921	0.402829	0.000000	129.29	333.69
	C	0.643921	-0.402829	0.000000	559.48	813.17
	O	-1.721263	-0.141348	0.000000	1064.79	1095.54
	O	1.721263	0.141348	0.000000	1339.47	1380.36
	H	-0.514710	1.497823	0.000000	1760.87	1779.11
	H	0.514710	-1.497823	0.000000	2985.56	2988.95
<i>syn</i> -1 $E = -227.57421$ ZPVE = 0.03664855 $E$ (total) = -227.53757	C	0.000000	0.768102	0.525590	85.74	280.82
	C	0.000000	-0.768102	0.525590	739.65	822.94
	O	0.000000	1.411476	-0.490596	848.95	1065.61
	O	0.000000	-1.411476	-0.490596	1393.09	1399.25
	H	0.000000	1.242891	1.524282	1768.83	1798.88
	H	0.000000	-1.242891	1.524282	2927.91	2955.19
2 $E = -227.55736$ ZPVE = 0.03733779 $E$ (total) = -227.52002	H	-1.615801	-0.041735	-0.793397	224.96	282.68
	C	-0.555145	0.010865	-0.597670	484.89	574.53
	C	-0.132309	0.007089	0.657853	678.98	1037.08
	O	0.222525	0.000246	1.767985	1181.14	1279.83
	O	0.366167	-0.062511	-1.636438	1430.27	2181.49
	H	0.463248	0.816154	-2.011865	3212.70	3820.86
3 $E = -227.50819$ ZPVE = 0.0369341 $E$ (total) = -227.47126	C	-0.599219	-0.009531	-0.021021	223.48	232.67
	C	0.599219	0.009531	-0.021021	285.49	346.37
	O	-1.922920	0.048051	-0.021021	354.97	799.34
	O	1.922920	-0.048051	-0.021021	1248.46	1284.69
	H	-2.258907	-0.619161	0.584157	1374.32	2434.65
	H	2.258907	0.619161	0.584157	3818.67	3820.32
4 $E = -227.42432$ ZPVE = 0.03451985 $E$ (total) = -227.3898	H	-0.458615	-0.859946	1.770221	179.44	219.68
	O	-0.473515	0.057967	1.465627	388.93	520.10
	O	0.647006	0.001413	0.501961	562.92	660.10
	C	0.136057	0.000603	-0.699389	784.87	1048.94
	C	-0.275850	-0.007288	-1.832353	1362.75	2189.77
	H	-0.629455	-0.002956	-2.833256	3473.19	3761.77

**ORCID iDs**

Jia Wang  <https://orcid.org/0000-0002-3795-8699>  
 Joshua H. Marks  <https://orcid.org/0000-0003-0492-2494>  
 Alexandre Bergantini  <https://orcid.org/0000-0003-2279-166X>  
 Ryan C. Fortenberry  <https://orcid.org/0000-0003-4716-8225>  
 Ralf I. Kaiser  <https://orcid.org/0000-0002-7233-7206>

**References**

- Abplanalp, M. J., Forstel, M., & Kaiser, R. I. 2016a, *CPL*, **644**, 79  
 Abplanalp, M. J., Gozem, S., Krylov, A. I., et al. 2016b, *PNAS*, **113**, 7727  
 Abplanalp, M. J., & Kaiser, R. I. 2019, *PCCP*, **21**, 16949  
 Adler, T. B., Knizia, G., & Werner, H.-J. 2007, *JChPh*, **127**, 221106  
 Bacmann, A., & Faure, A. 2016, *A&A*, **587**, A130  
 Ballotta, B., Martínez-Núñez, E., Rampino, S., & Barone, V. 2023, *PCCP*, **25**, 22840  
 Benner, S. A., Kim, H.-J., Kim, M.-J., & Ricardo, A. 2010, *Cold Spring Harb. Perspect. Biol.*, **2**, a003467  
 Bennett, C. J., Hama, T., Kim, Y. S., Kawasaki, M., & Kaiser, R. I. 2011, *ApJ*, **727**, 27  
 Bennett, C. J., Jamieson, C. S., Osamura, Y., & Kaiser, R. I. 2005, *ApJ*, **624**, 1097  
 Bennett, C. J., & Kaiser, R. I. 2007, *ApJ*, **661**, 899  
 Bouilloud, M., Fray, N., Benilan, Y., et al. 2015, *MNRAS*, **451**, 2145  
 Butscher, T., Duvernay, F., Rimola, A., Segado-Centellas, M., & Chiavassa, T. 2017, *PCCP*, **19**, 2857  
 Butscher, T., Duvernay, F., Theule, P., et al. 2015, *MNRAS*, **453**, 1587  
 Cernicharo, J., Marcelino, N., Roueff, E., et al. 2012, *ApJL*, **759**, L43  
 Chiar, J. E., Adamson, A. J., Kerr, T. H., & Whittet, D. C. B. 1995, *ApJ*, **455**, 234  
 Chuang, K.-J., Fedoseev, G., Qasim, D., et al. 2017, *MNRAS*, **467**, 2552  
 Clark, J. H., Moore, C. B., & Nogar, N. S. 1978, *JChPh*, **68**, 1264  
 Coggins, A. J., & Powner, M. W. 2017, *NatCh*, **9**, 310  
 Cooper, G., Reed, C., Nguyen, D., Carter, M., & Wang, Y. 2011, *PNAS*, **108**, 14015  
 Coutens, A., Loison, J.-C., Boulanger, A., et al. 2022, *A&A*, **660**, L6  
 da Silva, G. 2010, *AngCh*, **49**, 7523  
 de Barros, A. L. F., Mejía, C., Seperuelo Duarte, E., et al. 2022, *MNRAS*, **511**, 2491  
 de Marcellus, P., Meinert, C., Myrgorodska, I., et al. 2015, *PNAS*, **112**, 965  
 Drouin, D., Couture, A. R., Joly, D., et al. 2007, *Scanning*, **29**, 92  
 Eckhardt, A. K., Bergantini, A., Singh, S. K., Schreiner, P. R., & Kaiser, R. I. 2019, *AngCh*, **58**, 5663  
 Elango, M., Maciel, G. S., Palazzetti, F., Lombardi, A., & Aquilanti, V. 2010, *JPCA*, **114**, 9864  
 Enrique-Romero, J., Rimola, A., Ceccarelli, C., et al. 2022, *ApJS*, **259**, 39  
 Fedoseev, G., Cuppen, H. M., Ioppolo, S., Lamberts, T., & Linnartz, H. 2015, *MNRAS*, **448**, 1288  
 Fu, T.-M., Jacob, D. J., Wittrock, F., et al. 2008, *JGRD*, **113**, D15303  
 Gibb, E. L., Whittet, D. C. B., Schutte, W. A., et al. 2000, *ApJ*, **536**, 347  
 Hänni, N., Altwegg, K., Baklouti, D., et al. 2023, *A&A*, **678**, A22  
 Herbst, E., & Dishoeck, E. F. v. 2009, *ARA&A*, **47**, 427  
 Hollis, J. M., Lovas, F. J., & Jewell, P. R. 2000, *ApJ*, **540**, L107

- Hollis, J. M., Lovas, F. J., Jewell, P. R., & Coudert, L. H. 2002, *ApJ*, **571**, L59
- Hudson, R., & Moore, M. 1999, *Icar*, **140**, 451
- Hudson, R. L., Moore, M. H., & Cook, A. M. 2005, *AdSpR*, **36**, 184
- Jiménez-Escobar, A., Chen, Y. J., Ciaravella, A., et al. 2016, *ApJ*, **820**, 25
- Jones, B. M., & Kaiser, R. I. 2013, *JPCL*, **4**, 1965
- Kim, H.-J., Ricardo, A., Illangkoon, H. I., et al. 2011, *JChS*, **133**, 9457
- Kleimeier, N. F., Eckhardt, A. K., & Kaiser, R. I. 2021, *JChS*, **143**, 14009
- Kleimeier, N. F., Eckhardt, A. K., Schreiner, P. R., & Kaiser, R. I. 2020, *Chem*, **6**, 3385
- Kleimeier, N. F., & Kaiser, R. I. 2021, *ChPhC*, **22**, 1229
- Kleimeier, N. F., & Kaiser, R. I. 2022, *JPCL*, **13**, 229
- Knizia, G., Adler, T. B., & Werner, H.-J. 2009, *JChPh*, **130**, 054104
- Koch, D. M., Khieu, N. H., & Peslherbe, G. H. 2001, *JPCA*, **105**, 3598
- Larsen, R. W., Hegelund, F., Ceponkus, J., & Nelander, B. 2002, *JMoSp*, **211**, 127
- Larsen, R. W., Pawłowski, F., Hegelund, F., et al. 2003, *PCCP*, **5**, 5031
- Leroux, K., Guillemin, J.-C., & Krim, L. 2020, *MNRAS*, **491**, 289
- Leroux, K., Guillemin, J.-C., & Krim, L. 2021, *MNRAS*, **504**, 2181
- Lewars, E., & Bonnycastle, I. 1997, *JMoSt (Theochem)*, **418**, 17
- Liszt, H. S., Pety, J., Gerin, M., & Lucas, R. 2014, *A&A*, **564**, A64
- Maier, G., & Rohr, C. 1996, *Liebigs Annalen*, **1996**, 307
- Maity, S., Kaiser, R. I., & Jones, B. M. 2015, *PCCP*, **17**, 3081
- Mardyukov, A., Keul, F., & Schreiner, P. R. 2021, *AngCh*, **60**, 15313
- Mardyukov, A., Wende, R. C., & Schreiner, P. R. 2023, *ChCom*, **59**, 2596
- Marks, J. H., Wang, J., Kleimeier, N. F., et al. 2023, *AngCh*, **62**, e202218645
- McClure, M. K., Rocha, W. R. M., Pontoppidan, K. M., et al. 2023, *NatAs*, **7**, 431
- McGuire, B. A. 2022, *ApJS*, **259**, 30
- Melosso, M., Bizzocchi, L., Gazzeh, H., et al. 2022, *ChCom*, **58**, 2750
- Mielke, Z., Mucha, M., Bil, A., et al. 2008, *ChPhC*, **9**, 1774
- Milligan, D. E., & Jacox, M. E. 1964, *JChPh*, **41**, 3032
- Milligan, D. E., & Jacox, M. E. 1971, *JChPh*, **54**, 927
- Mó, O., Alkorta, I., Guillemin, J.-C., & Yáñez, M. 2023, *Theor. Chem. Acc.*, **142**, 28
- Öberg, K. I., Boogert, A. A., Pontoppidan, K. M., et al. 2011, *ApJ*, **740**, 109
- Peterson, K. A., Adler, T. B., & Werner, H.-J. 2008, *JChPh*, **128**, 084102
- Pipes, J. G., Roux, J. A., Smith, A. M., & Scott, H. E. 1978, *AIAAJ*, **16**, 984
- Ricardo, A., Carrigan, M. A., Olcott, A. N., & Benner, S. A. 2004, *Sci*, **303**, 196
- Rivilla, V. M., Beltrán, M. T., Vasyunin, A., et al. 2019, *MNRAS*, **483**, 806
- Rivilla, V. M., Colzi, L., Jiménez-Serra, I., et al. 2022, *ApJL*, **929**, L11
- Rösch, D., Caravan, R. L., Taatjes, C. A., et al. 2021, *JPCA*, **125**, 7920
- Roux, J. A., Wood, B. E., Smith, A. M., & Plyer, R. R. 1980, Arnold Engineering Development Center Report AEDC-TR-79-81, AEDC
- Schmidt, F., Swiderek, P., & Bredehöft, J. H. 2019, *ESC*, **3**, 1974
- Schreiner, P. R., Reisenauer, H. P., Ley, D., et al. 2011, *Sci*, **332**, 1300
- Singh, S. K., Fabian Kleimeier, N., Eckhardt, A. K., & Kaiser, R. I. 2022, *ApJ*, **941**, 103
- Snyder, L. E., Hollis, J. M., & Ulich, B. L. 1976, *ApJ*, **208**, L91
- Taatjes, C. A., Hansen, N., McIlroy, A., et al. 2005, *Sci*, **308**, 1887
- Terlouw, J. K., Burgers, P. C., Baar, B., Weiske, T., & Schwarz, H. 1986, *CHIMIA Int. J. Chem.*, **40**, 357
- Thi, W.-F., van Dishoeck, E. F., Dartois, E., et al. 2006, *A&A*, **449**, 251
- Tielens, A. G. G. M. 2013, *RvMP*, **85**, 1021
- Turner, A. M., Abplanalp, M. J., Blair, T. J., Dayuha, R., & Kaiser, R. I. 2018, *ApJS*, **234**, 6
- Turner, A. M., Abplanalp, M. J., Chen, S. Y., et al. 2015, *PCCP*, **17**, 27281
- Turner, A. M., Bergantini, A., Koutsogiannis, A. S., et al. 2021, *ApJ*, **916**, 74
- Turner, A. M., & Kaiser, R. I. 2020, *AcChR*, **53**, 2791
- Turner, A. M., Koutsogiannis, A. S., Kleimeier, N. F., et al. 2020, *ApJ*, **896**, 88
- Turner, B. E., & Apponi, A. J. 2001, *ApJ*, **561**, L207
- Verderame, F. D., Catellucci, E., & Califano, S. 1970, *JChPh*, **52**, 719
- Vijay, D., & Sastry, G. N. 2005, *JMoSt (Theochem)*, **714**, 199
- Wang, J., Li, Y., Zhang, T., et al. 2008, *ApJ*, **676**, 416
- Wang, J., Marks, J. H., Tuli, L. B., et al. 2022, *JPCA*, **126**, 9699
- Wang, J., Marks, J. H., Turner, A. M., et al. 2023a, *SciA*, **9**, eadg1134
- Wang, J., Marks, J. H., Turner, A. M., et al. 2023b, *PCCP*, **25**, 936
- Wang, J., Nikolayev, A. A., Zhang, C., et al. 2023c, *PCCP*, **25**, 17460
- Werner, H.-J., Knizia, P. J. K. G., Manby, F. R., et al. 2021, MOLPRO, Version 2021.2, a PACKAGE of Ab Initio Programs
- Whittet, D. C. B. 1997, *OLEB*, **27**, 101
- Woods, P. M., Slater, B., Raza, Z., et al. 2013, *ApJ*, **777**, 90
- Würmel, J., & Simmie, J. M. 2024, *Int. J. Chem. Kinet.*, **56**, 105
- Xiong, S.-Z., Yao, Q., Li, Z.-R., & Li, X.-Y. 2014, *CoFl*, **161**, 885
- Yeghikyan, A. G. 2011, *Ap*, **54**, 87
- Yousaf, K. E., & Peterson, K. A. 2008, *JChPh*, **129**, 184108
- Zheng, W., Jewitt, D., & Kaiser, R. I. 2006, *ApJ*, **639**, 534
- Zhu, C., Kleimeier, N. F., Turner, A. M., et al. 2022a, *PNAS*, **119**, e2111938119
- Zhu, C., Wang, H., Medvedkov, I., et al. 2022b, *JPCL*, **13**, 6875